

This is the preprint of the contribution published as:

Fricke, C., Klee, T., Richter, S., Paufler, S., Harms, H., Maskow, T. (2021):
Numerical heat flow and transport simulation as a development tool for the design of
isothermal microcalorimeters
Thermochim. Acta **706** , art. 179070

The publisher's version is available at:

<http://dx.doi.org/10.1016/j.tca.2021.179070>

Numerical heat flow and transport simulation as a development tool for the design of isothermal microcalorimeters

Christian Fricke¹, Toralf Klee², Sven Richter², Sven Paufler¹, Hauke Harms¹, Thomas Maskow¹

¹ Helmholtz Centre for Environmental Research – UFZ, Permoserstraße 15, 04318 Leipzig, Germany

² Loetec Elektronische Fertigungssysteme GmbH, Dresdener Straße 28, 06886 Lutherstadt Wittenberg

Abstract: Numerous processes in biology and chemistry are accompanied by heat emission or consumption, which can be measured by isothermal microcalorimetry in the nano- to microwatt range and used to quantify the corresponding stoichiometry and kinetics. Sometimes these applications require special isothermal microcalorimeter (IMC), which are unaffordable e.g. microbiological routine testing. The design, construction and optimization of an IMC can be tedious and cost-intensive. It is thus suggested to accelerate and fasten the development process by numerical simulation using the finite element method (FEM). The FEM provides a complete picture of all energy and material fluxes not only temporally but also spatially resolved, which are difficult to determine experimentally.

In the present work, numerical simulations starting from a rough computer design of an IMC test system were performed and combined with experimental investigations using a physical test system under laboratory conditions to better understand the heat flows in the IMC and to support the development process towards a high-performance customized IMC. A representative detailed 3D model of our physical test system was created and the numerical simulation results are compared by the measured data of the physical test system. Using our 3D numerical model, we can now simulate modifications to progressively enhance the performance of the current physical test system. We conclude that numerical simulations can help to reduce the time and costs associated with the development process of customised IMCs.

Keywords: Isothermal Microcalorimeter, CFD, heat flow and transfer, finite element method

Introduction

The development of high-performance isothermal microcalorimeters (IMCs) based on the heat conduction principle has a long tradition. The calorimeter developed first by Tian (1923) and further improved by Calvet (1948) can be seen as the beginning of modern IMCs [1-3]. The development process at that time is well documented by Calvet and Prat [4]. Since then several microcalorimeters for a wide variety of applications were designed and constructed [3, 5-12]. The focus of these works was on the design of components, the performance of heat flow sensors (tested by calibration) and the suppression of parasitic heat flows of the overall system [13-17]. Nowadays, hardly any making of process-specific calorimeters is described and the development of commercially available microcalorimeters is largely kept undisclosed [18] (except for those [19, 12]).

35 In general, an IMC is composed of a measurement unit that consists of three components: i) a
36 calorimetric vessel in which the investigated process takes place, ii) a heat sink whose temperature is
37 precisely regulated at the desired operating temperature and iii) a heat flow sensor, which links the vessel
38 and the heat sink [17, 20]. If there is a significant change in temperature caused by any physical,
39 chemical or biological reaction in the vessel, a temperature gradient is formed over the heat flow sensor
40 [1]. Heat flow from the vessel to the heat sink or vice versa correspond to an exothermic or an
41 endothermic reaction, respectively [5, 21]. Thermoelectric generators (*i.e.* thermopiles) were widely
42 employed as heat flow sensors [22]. To ensure measurements of heat flows in the range of a few
43 microwatts, the measurement unit has to be well isolated from the surrounding and parasitic heat flow
44 kept to a minimum. Besides, the temperature control unit has to precisely regulate the power output of
45 heating elements to achieve very accurate temperature stability [3].

46 Since the smallest temperature differences are measured, the temperature distribution in the entire
47 system plays a key role [19]. However, this is often difficult to capture during the construction process
48 due to the complexity of the calorimetric system and therefore only individual and local temperatures
49 of components can be measured by internal temperature probes (e.g. Pt100 sensors). Moreover, it may
50 prove difficult to quantify all relevant heat flow paths experimentally in full detail. To overcome this
51 bottleneck in the construction process of microcalorimeters, we propose to apply finite element method
52 (FEM) computational simulations as a development tool for IMCs. Briefly, in FEM the considered
53 object is split into many small but finite elements. For each element node, a set of ordinary and partial
54 differential equations (ODE and PDE) describing the underlying physical processes and characteristics
55 such as heat transfer, computation fluid flow (CFD), structural mechanics etc. are solved [23] based on
56 defined initial and boundary conditions [24].

57 Only a few published studies used numerical simulations to investigate heat transfer and temperature
58 distribution in microcalorimeters. For instance, Vilchiz et al. investigated the heat transfer during gas
59 dosing experiments in a 2D (two-dimensional) and 3D (three-dimensional) model of a Tian-Calvet
60 microcalorimeter [25]. In the numerical study of Koci et al., the calibration of a virtual 3D model of a
61 real isothermal heat flow calorimeter was simulated [26]. Gonzalez-Duran et al. performed numerical
62 CFD simulations of a 2D model to analyse the geometry of a combustion chamber for developing a
63 reference calorimeter [27]. These studies only addressed specific issues and selected components of the
64 respective instruments. To our knowledge, there are no numerical simulations that address the entire
65 complexity of an IMC, including the temperature control systems, and therefore might apply to any type
66 of customized IMC.

67 In order to examine the extent to which FEM can describe heat flows and temperature distributions in
68 an IMC and even be used for optimization, we developed a 3D numerical model in COMSOL
69 Multiphysics® and a corresponding real-world test system of an IMC specifically designed for
70 microbiological analysis. By performing numerical analyses of the 3D model and selected compounds
71 we were able to simulate the 3D temperature distribution in the entire calorimetric system and to test

72 modifications of the system. Comparison of the simulations with temperature measurements at selected
73 points verified the adequacy of our model. Based on the comprehensive insight into the temperature
74 distribution in the system we were able to analyse the weak points of the test system as well as to
75 gradually introduce improvements.

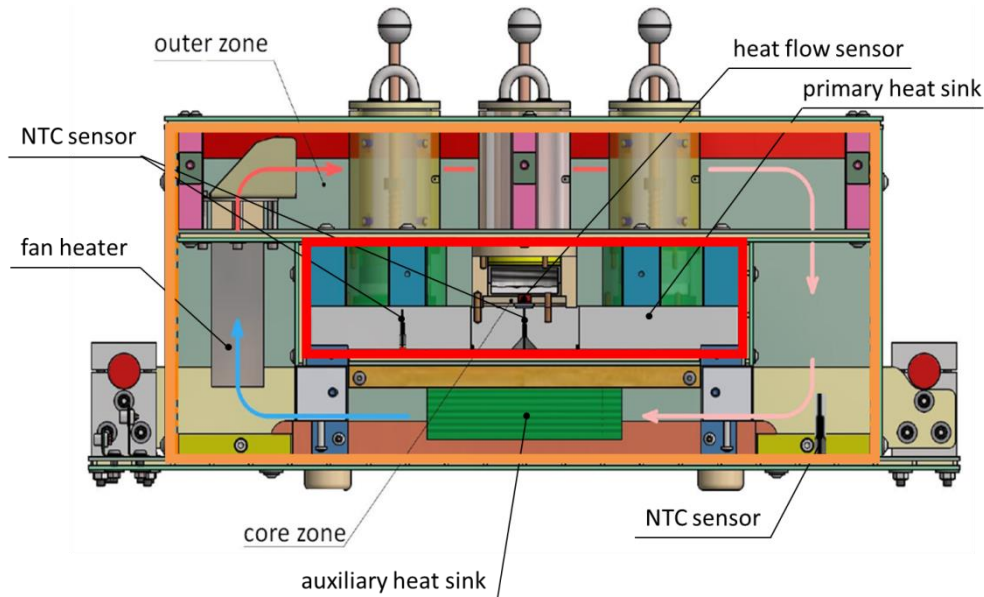
76 **Material and Methods**

77 **Design of the IMC-test system**

78 The studied IMC-test system (670 x 351 x 261 mm) was manufactured by KEK GmbH and Loetec
79 Elektronische Fertigungssysteme GmbH. That system is divided into two separate thermal zones to
80 shield the measuring point from environmental temperature fluctuations (schematic section through the
81 instrument in Fig. 1). The borders of the outer zone are indicated by orange lines and those of the core
82 zone by red lines. Arrows in the outer zone indicate the direction of airflow caused by an internal fan
83 heater (Piccovent 70 W, RO/SE Blechverarbeitung GmbH & Co. KG, Bad Birnbach, Germany). The air
84 domain in the outer zone is heated by the heating element of the fan (Fig. 1 left). This heating element
85 is regulated by a PID controller. The actual temperature in the outer zone is measured by an internal
86 negative temperature coefficient (NTC) sensor (Amphenol Advanced Sensors Germany GmbH,
87 Pforzheim, Germany), which is located on the lower right side of the test system. The operating
88 temperature is set to 37 °C which is routinely used for many applications in microbiological analysis.
89 The IMC-test system has three measuring channels (arranged in a row). Each channel consists of an
90 upper part (aluminium) containing the sample holder (polyamide, PA) and a lower part (PA). The latter
91 is located in the core zone directly on top of the primary aluminium heat sink (300 x 300 x 30 mm). This
92 lower part of the channel encloses the actual measuring unit, a high-performance heat flow sensor (TGP-
93 651, Micropelt GmbH, Freiburg, Germany). The bottom of the heat flow sensors is thermally bonded to
94 the primary heat sink which provides a constant reference temperature for the sensor elements. Petri
95 dish like sample containers of different sizes and geometry can be placed on the top of the sensors and
96 thus fulfil the criteria for conventional microbiological analysis. This makes the calorimeter particularly
97 suitable for the quantification of bacterial contamination in liquid media (e.g. tap water, process waters,
98 and juices) or also in extracts, which are important in the food industry, medicine or even pharmacy.
99 The calorimeter presented in this study is designed to reliably detect changes in the heat production rate
100 <1 mW, which is sufficient to rapidly detect the metabolic activity of common potential pathogens such
101 as *E. coli*, *L. pneumophila*, *S. aureus*, etc.

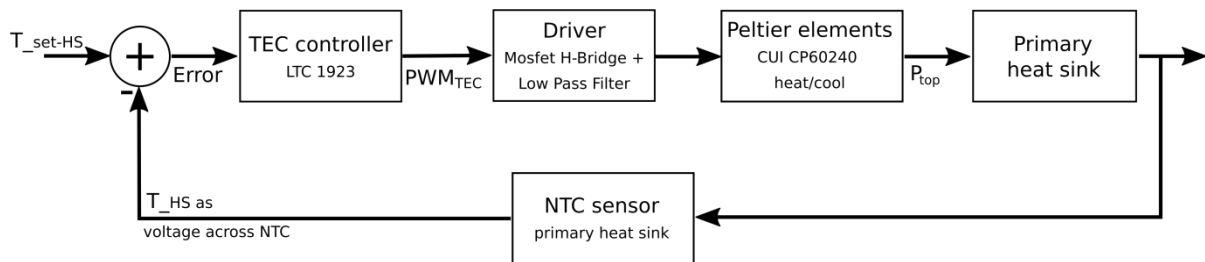
102 Both the core as well as the outer zone are surrounded by insulation plates (a sandwich construction
103 made out of acrylonitrile butadiene styrene, ABS, and air-filled honeycombs). The temperature of the
104 heat sink is controlled via a PID control loop using an NTC located directly below the central measuring
105 channel as a sensor and a thermoelectric cooler controller (LTC 1923, Linear Technology, Milpitas,
106 California, USA) with two Peltier modules (20 x 20 mm, CP60240, CUI Devices, Lake Oswego,

107 Oregon, USA) as an actuator. The signal flow diagram is shown in Fig. 2. An additional NTC sensor is
 108 located below channel 1. The heat generated on the opposite side by the Peltier module is dissipated via
 109 the auxiliary heat sink (138 x 50 mm, SK466, Fischer Elektronik GmbH & Co. KG, Lüdenscheid,
 110 Germany). In addition to those actuator Peltier modules, two heater foils (THF-5095, Reichelt
 111 Elektronik, Sande, Germany) are used to support the heat-up phase of the primary heat sink until the
 112 desired set temperature (37 °C) is reached (not shown in Fig. 1).



113
 114 **Figure 1:** Section through the IMC-test system (orange line – outer thermal zone, red line – inner thermal zone).

115 The data acquisition and control unit with a graphical user interface is located in an external module
 116 connected to the IMC-test system. Temperature values and voltages of all NTC sensors and heat flow
 117 sensors, respectively, are displayed numerically and graphically in real-time. All recorded data are stored
 118 in a database with the associated timestamp that can be assessed externally.



119
 120 **Figure 2:** Signal flow diagram of the control loop in the microcalorimetric test system using the TEC controller, which regulates
 121 the temperature on the primary heat sink.

122 Experimental procedure

123 Performance test

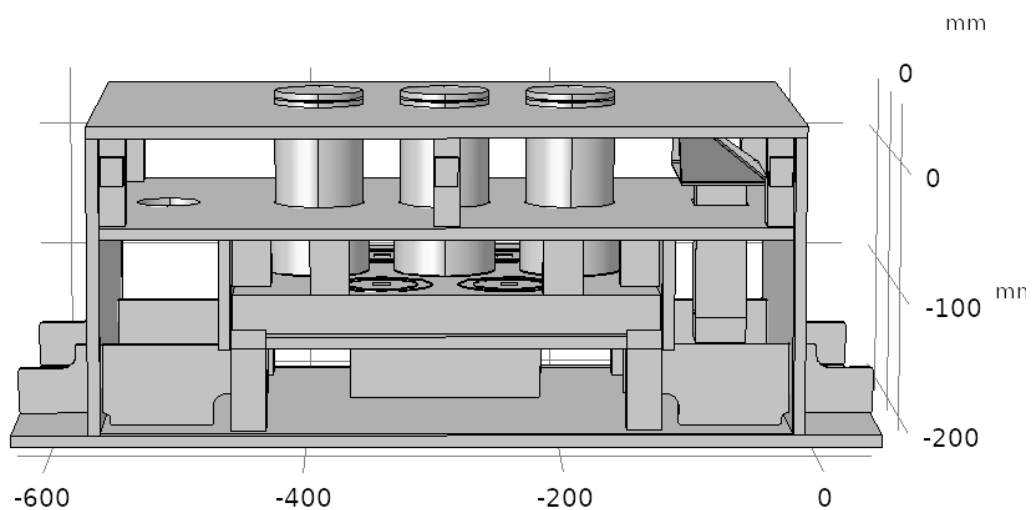
124 In order to determine the overall performance of the IMC test system, the calorimeter was run for approx.
 125 72 h (long-term response). All experiments started at room temperature (20 to 23 °C) to ensure equal
 126 starting conditions. During this test phase, the following parameters were determined: time to meet set-

127 temperature of air and heat sink, the temperature stability of the heat sink as well as the performance of
128 the heat flow sensors.

129 In addition to the three internal temperature measuring points, three flexibly positionable Pt100 sensors
130 (1/3 DIN 4-wire thin-film platinum sensors connected to the LabBox (HiTec Zang GmbH,
131 Herzogenrath, Germany)) were installed to measure the temperature profile at various points in the test
132 system. The calorimeter was again tested for approx. 6 h (short-term response, sufficient to reach
133 thermal equilibrium) starting at room temperature. In this way, we were able to roughly map the
134 temperature distribution in the test system. All data, both internal and external, were evaluated in
135 *OriginPro* 2018 (OriginLab Corporation, Northampton, USA). For details, see supplementary material,
136 SM.

137 Numerical model of the IMC-test system

138 The FEM simulations were run on COMSOL[®] Version 5.5 (COMSOL Multiphysics GmbH, Göttingen,
139 Germany). Fig. 3 illustrates the three-dimensional geometry reconstructed in the simulation software.
140 The material assignment of all components is given in Tab. S1 in the SM. All components have been
141 created true to scale from a CAD design. The dimensions of the individual components were determined
142 in Autodesk[®] *Inventor Professional 2017* (Autodesk, Mill Valley, California, USA) and incorporated as
143 input for the creation of the 3D model in the simulation software.



144
145 **Figure 3:** The geometry of the 3D numerical model. Insulation plates were removed to visualise the internal details of the 3D
146 model.

147 Nevertheless, the following simplifications were made: insulation plates were rebuilt only of one
148 material instead of an air-filled sandwich structure. Holes, screws, wires and bar magnets were
149 neglected. The sample holder structure was simplified through a cylindrical stopper. Heat flow sensors,
150 Peltier modules, heater foils and the air heater were reconstructed simplified. The interior fan is
151 displayed as a square surface at the lower end of the air heater. These simplifications and neglections
152 have two reasons. First, the elements have little or no influence on the physical properties of the system.

153 Second, these fragmented components exhibiting many small domains, which would increase the
 154 computation time enormously.

155 **Modelling and simulation**

156 The simulations were separated into two different phases. In the first phase, the performance and
 157 interactions of the most important components were studied focusing on the heat sink configuration and
 158 its temperature regulation via the Peltier modules and the respective feedback control loop (see chapters
 159 S4 and S5 in the SI). Here, the method for determining the control parameters is demonstrated. The
 160 obtained results are used for the control loop on the heat sink in the complete model simulation.
 161 Additionally, the temperature distribution in the upper part of the model was investigated in detail, as
 162 this strongly influences the behaviour of the measurement channels. For this purpose, the velocity
 163 magnitude of air flowing through the fan was first determined in a preliminary simulation (see for details
 164 chapter S6 in the SI). The numerical solution obtained then served as input for the simulations of the
 165 temperature distribution in the upper part.

166 The second phase analyses the temperature distribution of the complete test system. In particular, such
 167 temperature distributions are considered that cannot be obtained experimentally, such as on the heat sink
 168 or the cross-section through the entire test system. Therefore, all heating elements (see Tab. 1) and their
 169 control loops were included in the numerical simulation.

170

171 **Table 1:** Heat source components, their power output and control loop parameters applied in the numerical simulations

component	Parameters	controller	COMSOL implementation
Peltier ^a modules	$q_{\max} = 13.8 \text{ W}$, $q_{\min} = -13.8 \text{ W}$ $K_{p1} = 162$, $K_{i1} = 18$, $K_{d1} = 0$, $T_{r1}^c = 25 \text{ s}$, $T_{\text{set}1} = 310.22 \text{ K}$	PI	ODE and DAE interface, PID interface with domain point probe as input temperature
air heater ^b	$q_{\max} = 70 \text{ W}$, $q_{\min} = 0 \text{ W}$ $K_{p2} = 15.25$, $K_{i2} = 0.19375$ $K_{d2} = 75.5$, $T_{r2} = 5 \text{ s}$ $T_{\text{set}2} = 310.15 \text{ K}$	PID	ODE and DAE interface, PID interface with domain point probe as input temperature
heater foil	$q_{\text{on}} = 5 \text{ W const.}$	on-off	ODE and DAE interface, Event interface for on/off switch with domain probe as a temperature input

172 ^aPI controller parameters are determined in the present work.

173 ^bPID controller parameters were determined experimentally under laboratory conditions.

174 ^c time tracking constant

175

176 For simplicity, we assumed an on-off controller for the heating foils, although a PID controller was used
 177 in the test system because in practice the PID controller delivers almost 100% heating power below the
 178 setpoint and almost 0 % above it (see Fig. S4 in the SM).

179 For the consideration of all physical effects of influence, a programme in COMSOL using two interfaces
 180 was written. The airflow regime caused by an interior fan of the air thermostat was computed in
 181 stationary study steps using the *fluid flow* interface. For the sake of simplicity and to reduce
 182 computational effort, we assumed laminar flow. Heat transfer phenomena like conduction, natural and
 183 forced convection (the latter strongly occurred on the heat source of the fan heater) were mostly solved
 184 time-dependent in a second study step with the *heat transfer in solids and fluids* interface. Both
 185 interfaces are coupled in the *non-isothermal* interface. In the case of the upper part, we performed one-
 186 way coupled stationary studies of laminar flow and heat transfer, to reduce the computational time [28].

187 **Governing equations and boundary conditions**

188 ***Solid physics - Heat Transfer***

189 Solid physics are restricted to the *heat transfer* interface. The conductive heat flux is assumed to
 190 dominate and to obey Fourier's law:

$$191 \quad q = -k\nabla T \quad (1)$$

192 Where k is the thermal conductivity (in $\text{W}\cdot\text{m}^{-1}\cdot\text{K}^{-1}$), q is the heat flux (in $\text{W}\cdot\text{m}^{-2}$) and ∇T is the
 193 temperature gradient (in $\text{K}\cdot\text{m}^{-1}$). The development of the temperature field is computed by solving the
 194 heat balance:

$$195 \quad \rho C_p \frac{\partial T}{\partial t} = \nabla \cdot (k\nabla T) + Q \quad (2)$$

196 Where ρ is the density (in $\text{kg}\cdot\text{m}^{-3}$), C_p the specific heat capacity ($\text{J}\cdot\text{kg}^{-1}\cdot\text{K}^{-1}$), and Q the sum of heat
 197 sources (in $\text{W}\cdot\text{m}^{-3}$). All material-dependent constants used are provided in Tab. S1 in the SM. Potential
 198 contributions of heat radiation are neglected. The following initial and boundary conditions were
 199 defined. The initial temperature was set to 294.15 K (ambient temperature under laboratory conditions).
 200 The heat exchange with the environment is assumed as convective heat flux q_0 (in $\text{W}\cdot\text{m}^{-2}$, eq. 3).

$$201 \quad q_0 = h \cdot (T_{\text{ext}} - T) \quad (3)$$

202 Where h is the heat transfer coefficient (in $\text{W}\cdot\text{m}^{-2}\cdot\text{K}^{-1}$) and T_{ext} the external temperature (in K). In order
 203 to model laboratory conditions, h and T_{ext} were parameterized to $20 \text{ W}\cdot\text{m}^{-2}\cdot\text{K}^{-1}$ [25] and 294.15 K. All
 204 heat sources were assigned by a heat rate P_0 (in W) that corresponds to the regulated power output. In
 205 the case of the air heater and the Peltier modules, the heat rate is a variable of the implemented controller
 206 algorithm (see Tab.1).

207 ***Fluid physics - Laminar Flow***

208 The physics of fluid motions are described by the Navier-Stokes equation (eq. 4, conservation of
 209 momentum). By solving this equation together with the continuity equation (eq. 5, conservation of mass)
 210 and the energy equation (eq. 6, conservation of energy) we can predict the air velocity, pressure and
 211 temperature in our numerical model. To simplify the complex nature of fluid dynamics in our numerical

212 model, we made the following assumptions in respect to the fluid flow regime: i) incompressible, ii)
 213 laminar and iii) steady. These assumptions were made mainly to reduce the computation time and to
 214 achieve convergence of the numerical model. Further assumptions are made regarding the
 215 incompressibility (see below). Viscous heating is neglected.

$$216 \quad \rho \mathbf{u} \cdot \nabla(\mathbf{u}) = -\nabla p + \mu \nabla^2 \mathbf{u} + F \quad (4)$$

$$217 \quad \nabla \cdot \mathbf{u} = 0 \quad (5)$$

$$218 \quad \rho C_p \frac{\partial T}{\partial t} + \rho C_p \mathbf{u} \cdot \nabla T = \nabla \cdot (k \nabla T) + Q \quad (6)$$

219 Where ρ (in $\text{kg} \cdot \text{m}^{-3}$), u (in m/s), p (in Pa) and μ (in $\text{Pa} \cdot \text{s}$), C_p (in $\text{J} \cdot \text{kg}^{-1} \cdot \text{K}^{-1}$), k (in $\text{W} \cdot \text{m}^{-1} \cdot \text{K}^{-1}$) are the fluid
 220 density, velocity, pressure, dynamic viscosity, specific heat capacity and thermal conductivity,
 221 respectively. T stands for the temperature. F and Q represent the volume force as well as the sum of all
 222 heat sources.

223 The fluid velocity is formed on the interior fan. The fan is defined as an interior boundary, which is
 224 composed of an in- and outlet [29]. Here, a pressure difference between the inlet and outlet of the fan
 225 caused the fluid velocity (eq. 7). The pressure difference is a function of static pressure, p_{nf} (in Pa) as
 226 well as flow rate, $V_{0,\text{fd}}$ (in $\text{m}^3 \cdot \text{s}^{-1}$).

$$227 \quad \Delta p_{\text{pc}} = f(p_{\text{nf}}, V_{0,\text{fd}}) = [p - n^T \text{Kn} + \rho(\mathbf{u} \cdot \mathbf{n})^2]^{\pm} \quad (7)$$

228 Where \mathbf{n} is the normal vector, ρ (in $\text{kg} \cdot \text{m}^{-3}$) the density, p (in Pa) the pressure. Both parameters were
 229 taken over from the datasheet of the fan (MagLev Motor fan, MF40202V1-1000U-A99, Sunon,
 230 Kaohsiung, Taiwan). We added an additional pressure point constraint to the air domain to define the
 231 reference pressure p_0 . Again, to obtain a unique numerical solution by solving the eq. 4-6 for our
 232 numerical model, we have to determine initial and boundary conditions. The velocity field $\mathbf{u}(t=0)$, as
 233 well as the reference pressure $p_0(t=0)$, was initially set to 0. Finally, by default settings, the no-slip
 234 boundary condition (eq. 8) on the walls is applied.

$$235 \quad \mathbf{u} = 0 \quad (8)$$

236 This boundary condition considers that the velocity of the air domain becomes zero at the boundary.
 237 Due to the different heat sources, forced and natural convection is occurring in the fluid flow regime.
 238 Natural convection occurs through density variations caused by different temperature fields in the air
 239 domain. The latter phenomenon cannot physically be described by eq. 4. However, when gravity is
 240 considered, the Navier-Stokes equation is extended through the buoyancy force:

$$241 \quad \rho \mathbf{u} \cdot \nabla(\mathbf{u}) = -\nabla p + \mu \nabla^2 \mathbf{u} + \rho \mathbf{g} \quad (9)$$

242 Using the Boussinesq-approximation (a detailed derivation is found in [30]) density variations in the
 243 buoyancy term can be considered and the Navier-Stokes equation leads to:

$$244 \quad \rho_0 \mathbf{u} \cdot \nabla(\mathbf{u}) = -\nabla P + \mu \nabla^2 \mathbf{u} - \rho_0 \frac{T-T_0}{T_0} \mathbf{g} \quad (10)$$

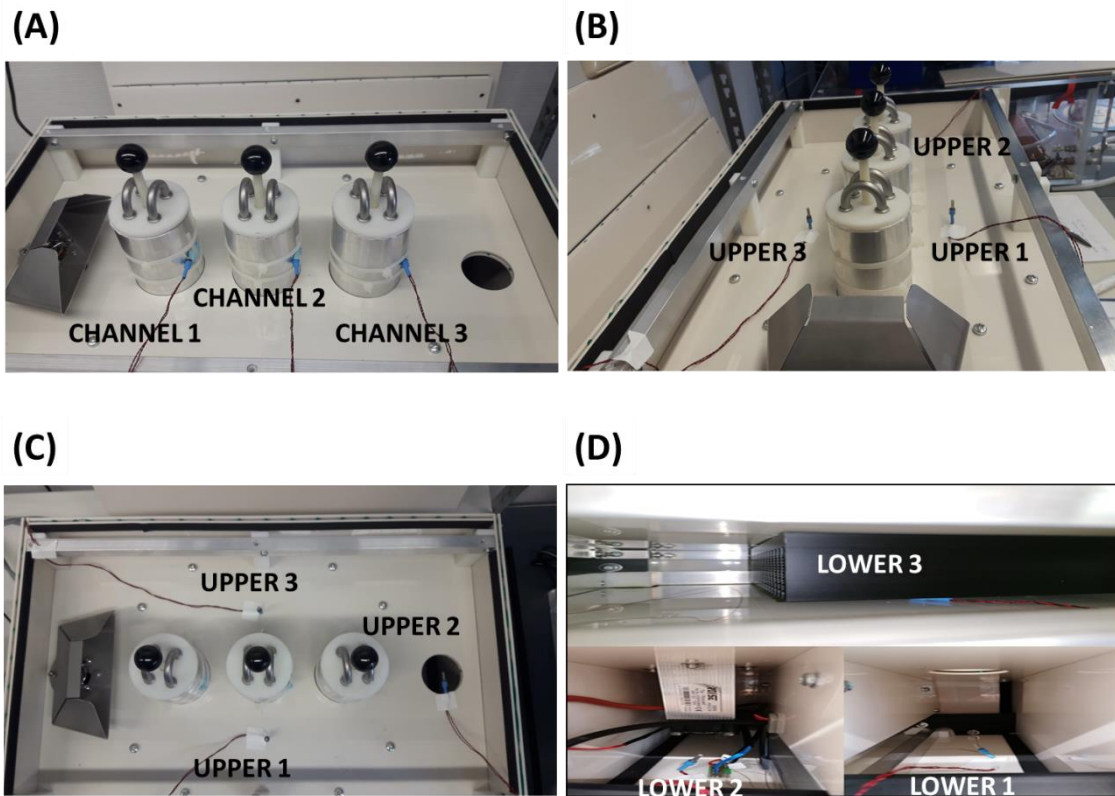
245 Where ρ_0 is the reference density (in $\text{kg}\cdot\text{m}^{-3}$), T_0 the reference temperature (in K), g the gravitational
 246 constant, P represents the pressure shift (in Pa) expressed by the elevation h (in m):

$$247 \quad P = p + \rho_0 g h \quad (11)$$

248 Results and discussion

249 Experimental performance test of the test system

250 To investigate the overall performance of the test system, we evaluated the data obtained from the
 251 internal sensors (temperature and heat flow sensors) as well as from the supplementary (external) Pt100
 252 sensors. In total, we measured the local temperature at 12 different positions (all external positions are
 253 displayed in Fig. 4) and the generated voltage of the heat flow sensors. The obtained data were compared
 254 with the simulation results to validate the 3D numerical model.



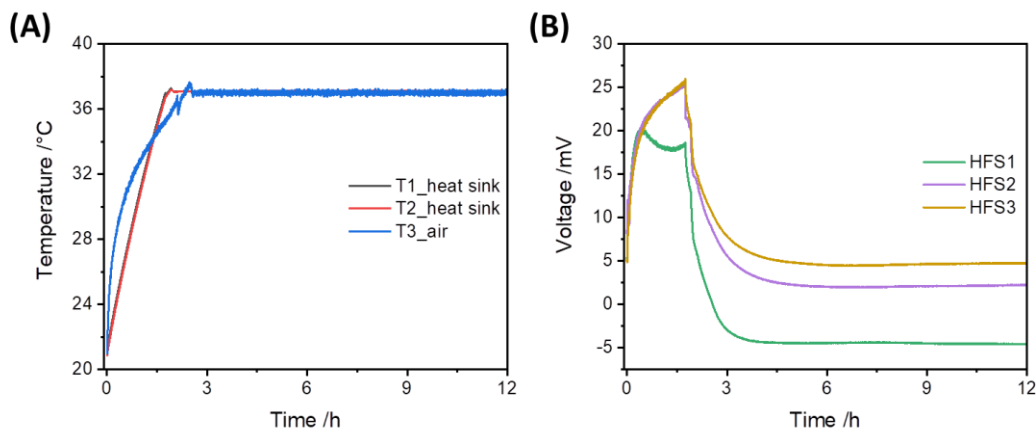
255
 256 **Figure 4:** Positions of all external temperature sensors located in the test system. **A):** Location of the Pt100 sensors connected
 257 to the channels. **B and C):** Location of the Pt100 sensors in the upper part of the test system. **D):** Location of the Pt100 sensors
 258 in the lower part of the test system.

259 **Evaluation of internal sensors**

260 Based on the signal flow diagram in Fig. 2, the measured temperatures on the heat sink and in the air
 261 domain were evaluated. The obtained temperature profiles are shown in Fig. 5A and the most valuable
 262 data (the heat flow) that can be internally extracted is the voltage of the heat flow sensors (HFS, Fig.
 263 5B). The voltage signal from the heat flow sensors U_{HFS} (in V) is given by:

264
$$U_{\text{HFS}} = \Delta T_{\text{HFS}} \cdot \alpha \quad (11)$$

265 Where α (in $\text{V} \cdot \text{K}^{-1}$) is the Seebeck coefficient and ΔT_{HFS} (in K) the temperature difference between the
 266 top and bottom of the HFS. Consequentially, the resulting voltage depends on material properties and
 267 the temperature gradient above the sensor. Since α is a constant it becomes obvious that fluctuations in
 268 the sensor signal are caused by temperature fluctuations occurring on the heat sink (in contact with the
 269 bottom side of the sensor) and the temperature of the air in the measuring chamber (in contact with the
 270 sensors top side). The desired operating temperature of 37°C was achieved after approx. 3 h (see Fig.
 271 5A). The mean air temperature (after thermal equilibration, considered time interval 6 to 72 h) was
 272 $(37.00 \pm 0.08)^\circ\text{C}$. The mean heat sink temperature measured at the two NTC sensors (after thermal
 273 equilibration, considered time interval 6 to 72 h) were $(37.072 \pm 0.001)^\circ\text{C}$ and $(37.107 \pm 0.001)^\circ\text{C}$ (for
 274 details see SM).



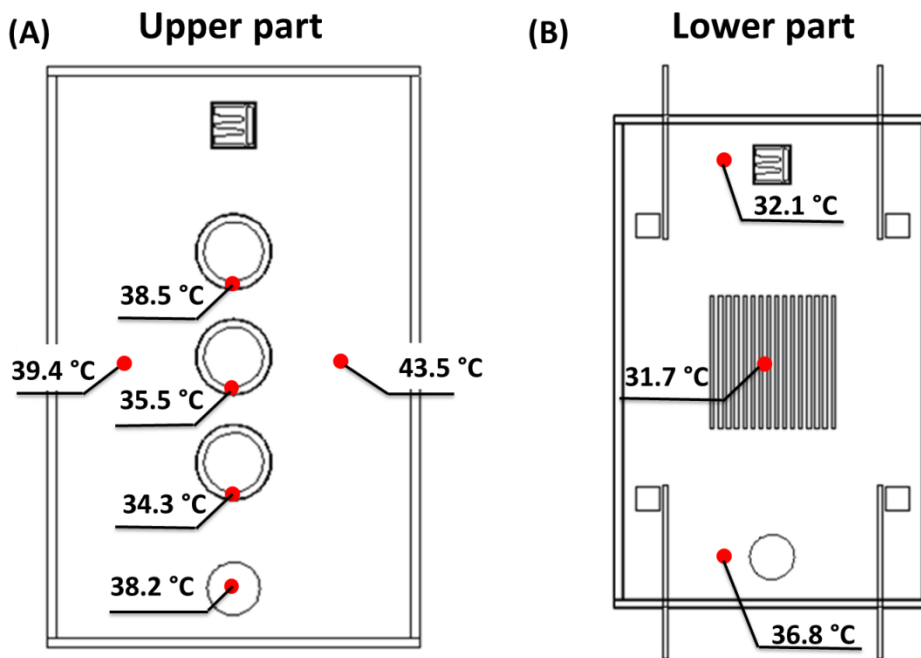
275 **Figure 5:** Summary of all obtained data from the internal sensors during the run-in phase of the test system. **A:** Temperature
 276 on the primary heat sink (T1_heat sink, black curve and T2_heat sink red curve) and of the flowing air (T3_air, blue curve). **B:**
 277 Generated voltage on the heat flow sensors (HFS1 green curve, HFS2, purple curve and HFS3 yellow curve).
 278

279 After approx. 6 h, a constant baseline at each HFS was achieved. Interestingly, the mean voltage signal
 280 varied strongly among the different HFS. The voltage profiles of HFS2 and 3 are almost equal. However,
 281 HFS1 showed the opposite profile. Even the sign between HFS1 as well as HFS2 and 3 is different. In
 282 general, two issues are affecting the generated voltages at the HFS. First, as mentioned earlier, there are
 283 time-dependent variations in temperature that have a direct impact on the variation of the voltage over
 284 time (detailed evaluation is given in the SI). In order to minimize such variations, better insulation to
 285 the environment and improved control of the temperature in the outer zone can be used. Second, signal
 286 differences between the three HFS are caused by spatial temperature gradients. Since U_{HFS} is

287 proportional to ΔT_{HFS} (see eq. 11), we can calculate ΔT_{HFS} by using the Seebeck coefficient of the TEGs
 288 ($\alpha = 60 \text{ mV}\cdot\text{K}^{-1}$). As a result, we obtained temperature differences for HFS 1 of -80 mK (the top is
 289 warmer than the bottom side), for HFS 2 of +40 mK and for HFS 3 of +100 mK (in both cases is the top
 290 colder than the bottom side). Unfortunately, from our experimental data, we cannot localize the cause
 291 of these temperature differences among the HFS. Therefore, FEM simulations are crucial to visualize
 292 spatial temperature gradients on the one hand and to test solutions by simulations in advance to improve
 293 the spatial temperature distribution on the other hand. The different voltage profiles, as well as the
 294 differences in temperature between the heat flow sensors, will be explained in more detail when we
 295 consider the corresponding heat transfer simulation results.

296 Evaluation of external sensors

297 Even if the internal data already revealed some information about the temperature distribution, this
 298 information is mainly restricted to the inner zone of the test system. To obtain local temperatures in the
 299 outer zone, we added external Pt100 sensors (see locations in Fig. 4). The mean steady-state
 300 temperatures for the measuring point are mapped in Fig. 6. The corresponding temperature profiles are
 301 given in the SM. By using the external sensors we get a more accurate estimation of the performance of
 302 the test system and at the same time, we can use the measured temperatures for the validation of our
 303 numerical model. By solving the heat transfer and fluid flow equations numerically in our 3D model,
 304 we can explain the underlying causes of the measured effects by the internal and external sensors.



305
 306 **Figure 6:** Steady-state temperatures of all external Pt100 sensors in the IMC test system. **A:** Local temperatures in the upper
 307 part. Three sensors were placed on the wall of the channels. Two sensors were located next to the reference (Ch2) channel and
 308 a third sensor was placed in the centre of the transition between the upper and lower part. **B:** Local temperatures in the lower
 309 part. One sensor was located below the auxiliary heat sink. The second sensor was placed next to the internal NTC sensor that
 310 measures the temperature in the outer zone and the third sensor was placed on at the level of the fan.

311 Figure 6 shows large temperature differences ranging from 31.7 °C (in the outer zone, lower part) to
 312 43.5 °C (in the upper part, next to the reference channel 2). The lowest temperature (31.7 °C) is caused

313 by the Peltier modules that regulate the temperature of the primary heat sink. Since this cool spot is
314 below the core zone no influence on the performance of the overall IMC system is expected. However,
315 strong temperature differences were also observed in the upper part. Depending on the location of the
316 external Pt100 sensor (at the level of channel 2), temperature differences (in steady-state) of 4 °C were
317 observed (39.4 °C left side vs. 43.5 °C right side). Again, we will discuss the influence of these
318 deviations on the overall system in the context of the numerical simulation results. The temperature
319 difference between channel 1 and channel 2 or 3 can simply be explained by the lateral arrangement of
320 the channels related to the fan heater.

321 **Numerical results**

322 As the test system is restricted to three internal temperature probes that are used as input signals for the
323 temperature control loops. Only at those three discrete points, the temperature can be measured to
324 characterize the system. Consequentially, spatial temperature gradients, heat accumulations and thermal
325 bridges cannot be detected system-wide without installing additional sensors. However, all these
326 phenomena affect directly the performance and thus the sensitivity of heat flow measurements by the
327 sensors. Especially, variances regarding voltage signals between heat flow sensors remain inexplicable.
328 In the following, numerical results from two selected models are presented. In order to understand the
329 different behaviour of the heat flow sensors (see data obtained under laboratory conditions, Fig. 5B),
330 heat flow and transfer simulations of the upper part are conducted. Additionally, modifications of the
331 upper part are simulated in advance to demonstrate the predictive power of numerical simulations.
332 Finally, to get insight into the overall temperature distribution, the complete model was solved
333 numerically. Here, control parameters obtained from simulations of the control loop of the heat sink (see
334 chapter S4 and S5 in the SI) are used for this simulation. To validate our numerical results temperatures
335 are compared with experimental data.

336 **Temperature distribution in the upper part**

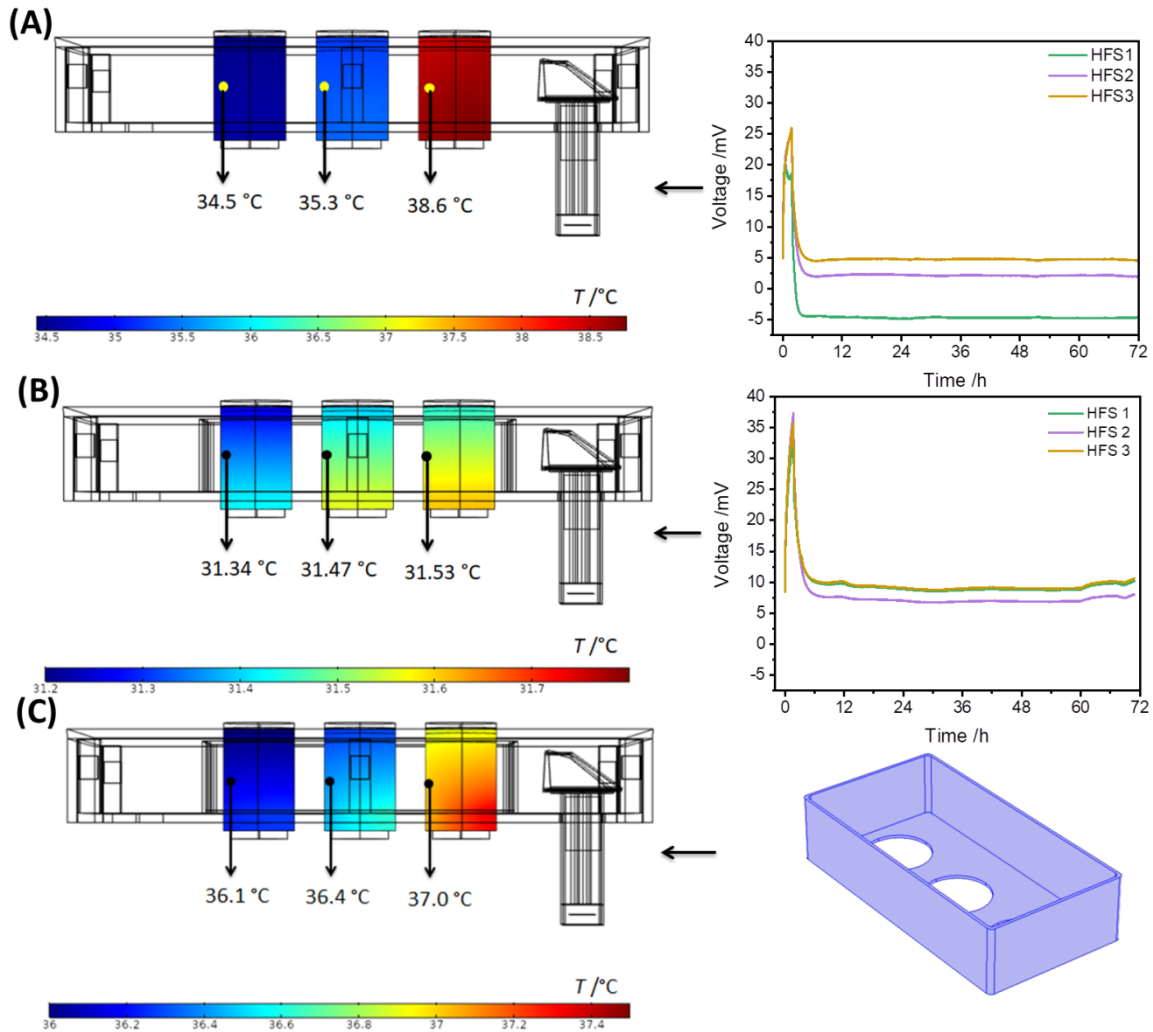
337 As the experimental data already revealed, strong temperature gradients can be observed in the upper
338 part of the IMC test system (see Fig. 6A). Since the temperature of the channels has a significant effect
339 on the heat flow sensors, simulations were performed on the upper part of the calorimetric system. The
340 numerical results are validated by experimental data and possible modifications in the upper part are
341 simulated with the aim of lower temperature differences between the channels and thus more equal
342 responses of the heat flow sensor.

343 In a preliminary study, the velocity magnitude v (in $\text{m}\cdot\text{s}^{-1}$, the magnitude of the velocity vector u) on the
344 boundary condition that represents the interior fan in our numerical model was determined (for details
345 see SI). Through this study, we were able to implement the average velocity magnitude $v = 4.2 \text{ m}\cdot\text{s}^{-1}$ as
346 an inlet boundary condition at the height of the fan position. Thereby, we simplified the entire simulation
347 to the upper part without having to recreate the complete airflow in the test system. Consequentially, an
348 outlet boundary condition was set at the transition between the upper and lower part. The considered

349 geometry of the upper part of the calorimeter is shown in Fig. 7. In a stationary study, the local
350 temperature distribution was simulated with particular emphasis on the temperature profiles of the
351 channels.

352 The temperature distribution across the channels for the initial test system is shown in Fig. 7A. The
353 numerical results are in good agreement with the experimental data and confirm the validity of the
354 simulated numerical model. Deviation between simulation and experimental data is only 0.2 °C (Fig.
355 7A). Those deviations can be attributed to (i) non-ideal heat flux boundary conditions, since under
356 laboratory conditions ambient temperature may vary with time. (ii) The influence of the necessary
357 simplifications concerning geometry and airflow (laminar flow and incompressible fluid). (iii) The mesh
358 might be too coarse, thus strong gradients, as they occur especially at the heating element of the fan,
359 cannot be modelled perfectly. The latter reason can be largely excluded because the simulations were
360 carried out exemplarily with different meshes. Due to the accuracy of our model, we can simulate
361 specific modifications to achieve a more uniform temperature distribution across the channels. The first
362 approach is the protection of the channels by an aluminium shield (300 x 150 x 70 mm) with a thickness
363 of 3 mm around the channels (see Fig 7C). The corresponding numerical solution (Fig. 7B) shows a
364 much more uniform temperature distribution. However, the simulated temperature (approx. 31.5 °C) is
365 far away from the desired temperature (37 °C).

366



367

368 **Figure 7:** Numerical solutions of the temperature distribution among the channels obtained from the one-way coupled
 369 stationary studies. **A:** Temperature volume plots of the channels in the original reconstruction of the upper part. Next to it, the
 370 experimentally measured voltage curves in this configuration **B:** Temperature volume plots of the channels in a modified
 371 reconstruction of the upper part by adding a frame around the channels. Next to it, the experimentally measured voltage curves
 372 in this modified configuration **C:** Temperature volume plots of the channels in a modified reconstruction of the upper part by
 373 adding a frame with a bottom plate around the channels. Next to it, the geometry of this frame with the bottom plate.

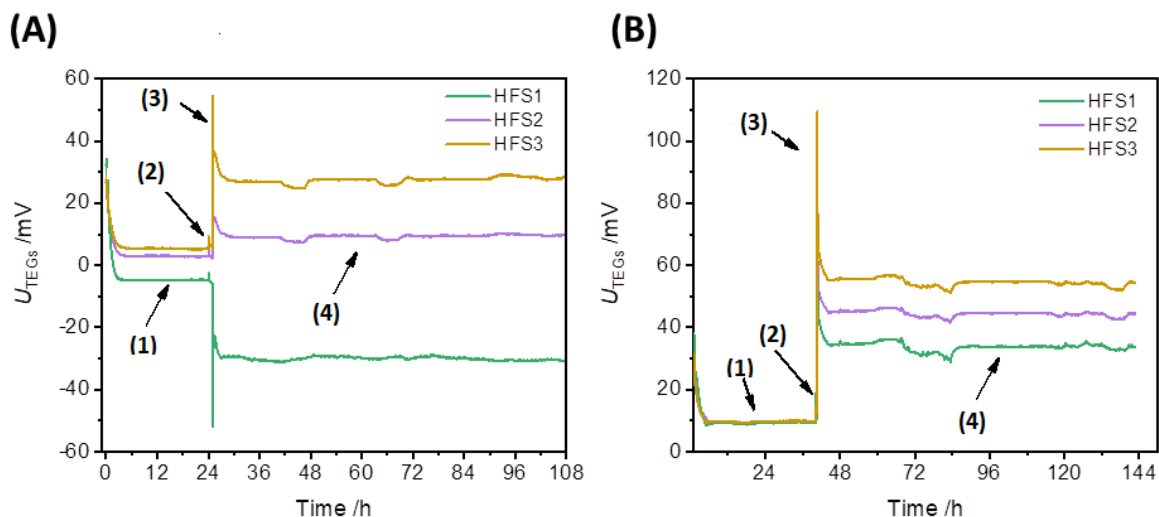
374 Experimental data of this configuration confirms the simulation with a temperature difference among
 375 the channels of approx. 1 °C ($T_{ch1} = 33.5$ °C, $T_{ch3} = 32.7$ °C, $T_{ch2} = 32.4$ °C). This behavior can be
 376 attributed to the fact that by inserting the frame, the channels are surrounded by stagnant air, which is a
 377 poor heat conductor. However, this modification leads also to a drastically reduced difference in the
 378 generated voltage by the heat flow sensor performance. Moreover, by the fact that the channels are now
 379 colder, the offset of the voltage is correspondingly higher, which correlated very well with the
 380 experimental data (see Fig.7B). Here, one possibility might be to change the position of the temperature
 381 probe in close contact with the aluminium shield.

382 To overcome this temperature issue, we simulated in another study a modified frame with a 3 mm thick
 383 bottom plate as a heat conductor (geometry is shown in Fig. 7C). This time, we achieved a temperature
 384 difference of 0.9 °C (Fig. 7C) which is slightly worse than the solution without the bottom plate (0.2
 385 °C) but deviates from the desired temperature of 37 °C by only approx. 0.6 to 0.9 °C. Further approaches

386 and modifications can easily be simulated on this model to optimize the temperature value and
387 variations.

388 In order to determine the influence of calorimetric vessels ($V = 35 \text{ mL}$, $d = 50 \text{ mm}$, $h = 19 \text{ mm}$) and
389 additional heat shields (aluminium frame around the channels), we measured the heat signal without
390 (Fig. 8A) and with (Fig. 8B) frame and added empty calorimetric vessels at the time (2) in the pre-
391 temperature position and at time (3) finally on the heat flow sensor. In the most cases, the voltage signal
392 increased after insertion of the calorimetric vessel, indicating a temperature gradient within the air space
393 in the lower part of the measuring channel (detailed information are given in the next section). For
394 quantitative evaluation of the influence of the frame, the baseline ΔU_{HFS} for both measuring channels
395 (HFS1 and HFS3) was calculated as signal difference related to the reference channel (HFS2). The
396 standard deviation (SD) of ΔU_{HFS} was without frame (HFS1: 0.85 mV; HFS3: 0.34 mV or HSF1:
397 0.51 mW; HSF3: 0.20 mW) significantly higher as with frame (HFS1: 0.57 mV; HSF3: 0.25 mV or
398 HSF1: 0.34 mW; HSF3: 0.15 mW). For the calculation of SD, all data after insertion of the calorimetric
399 chamber on the thermal sensor (30 to 108 h without frame; 50 to 142.7 h with frame) were considered.
400 The estimation of the heat flows assumes the applicability of the theoretical calibration coefficient (ϵ_{theo}
401 $= 0.60 \text{ W} \cdot \text{V}^{-1}$, all heat goes through the sensor). If we require 3 times the SD for reliable detection of
402 the heat production rate, then 1 mW is achievable with the developed calorimeter supplemented by the
403 aluminium frame. However, follow-up studies on the calorimeter should address experimentally
404 determined calibration constant ϵ_{exp} for each measuring channel.

405



406

407 **Figure 8:** Experimentally measured heat flows (as raw voltage signal) without (A) and with frame (B). The arrows indicates
 408 (1): baseline period without calorimetric vessel, (2): insertion of the calorimetric vessel in pre-tempering position, resulting in
 409 slight signal increase, (3): insertion of the calorimetric vessel in measuring position, resulting in a higher signal due to thermal
 410 equilibration. (4) baseline period with calorimetric vessel in measuring position.

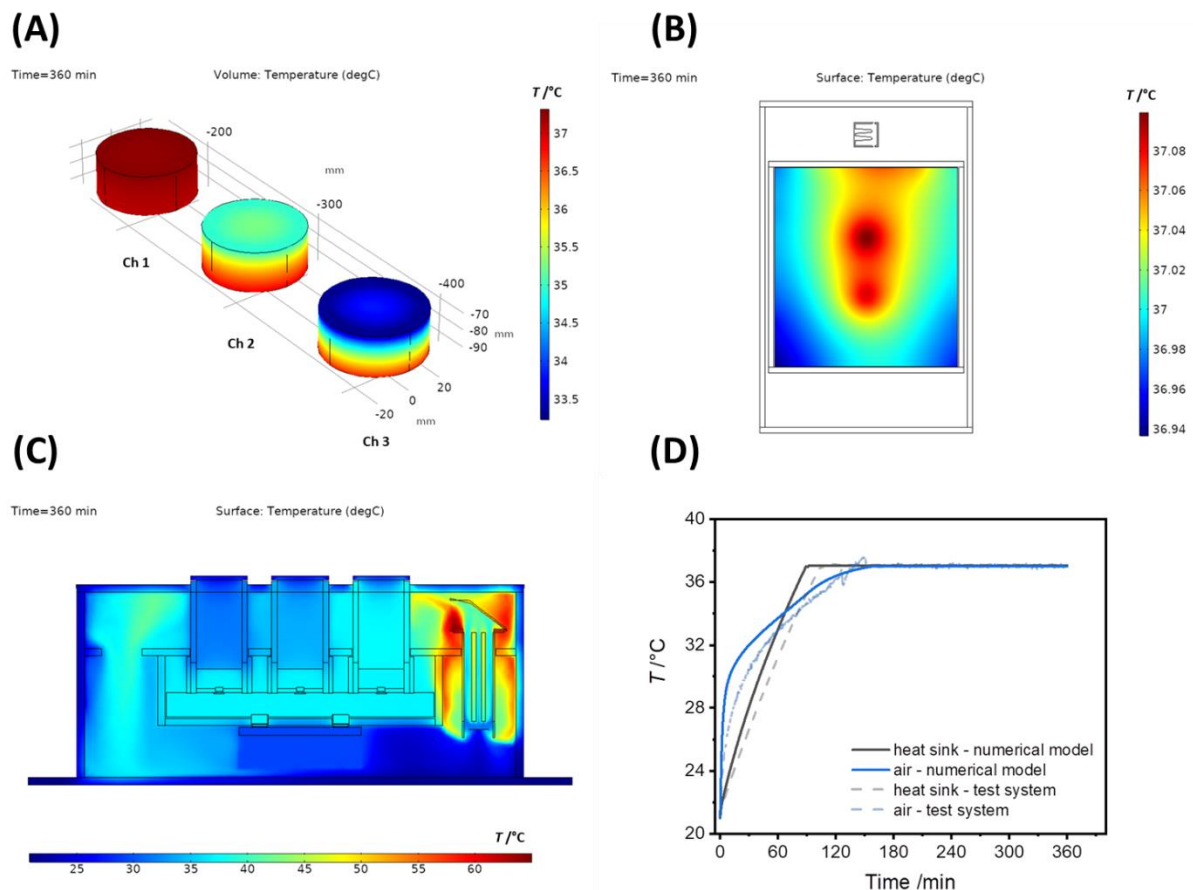
411 Heat transfer and fluid flow simulations of the complete model

412 In a final simulation, we reconstructed a complete 3D model of the initial test system (without any
 413 modifications) in the simulation software (see Fig. 3) and performed numerical simulations to
 414 investigate the overall temperature distribution. A particular selection of the simulation results is
 415 gathered in Fig. 9 and 10.

416 In Fig. 9 volume and surface plots of the temperature distribution of selected compounds or parts of the
 417 test system in 2 and 3D models are displayed. Additionally, the simulated temperature profile in the
 418 outer zone and on the heat sink are compared with the experimental data (Fig. 9D). Fig. 9A shows the
 419 simulated temperature variations across the channels in which the samples are finally placed on the heat
 420 flow sensors. Based on these temperature plots, we can easily explain the observed different behavior
 421 of the heat flow sensors (Fig. 5B and 8A, B). Additionally, entering a sample vessel into the measuring
 422 position should increase the voltage signal of the heat flow sensors, since the temperature gradient in
 423 the measuring chamber is transferred to the sample vessel. We observed exactly this behavior in
 424 experiments under laboratory conditions (Fig. 8).

425 Fig. 9B shows a surface plot of the temperature distribution of the heat sink. The asymmetric temperature
 426 distribution can be explained by the heat released by the fan heater (hot spot on the right side in Fig.

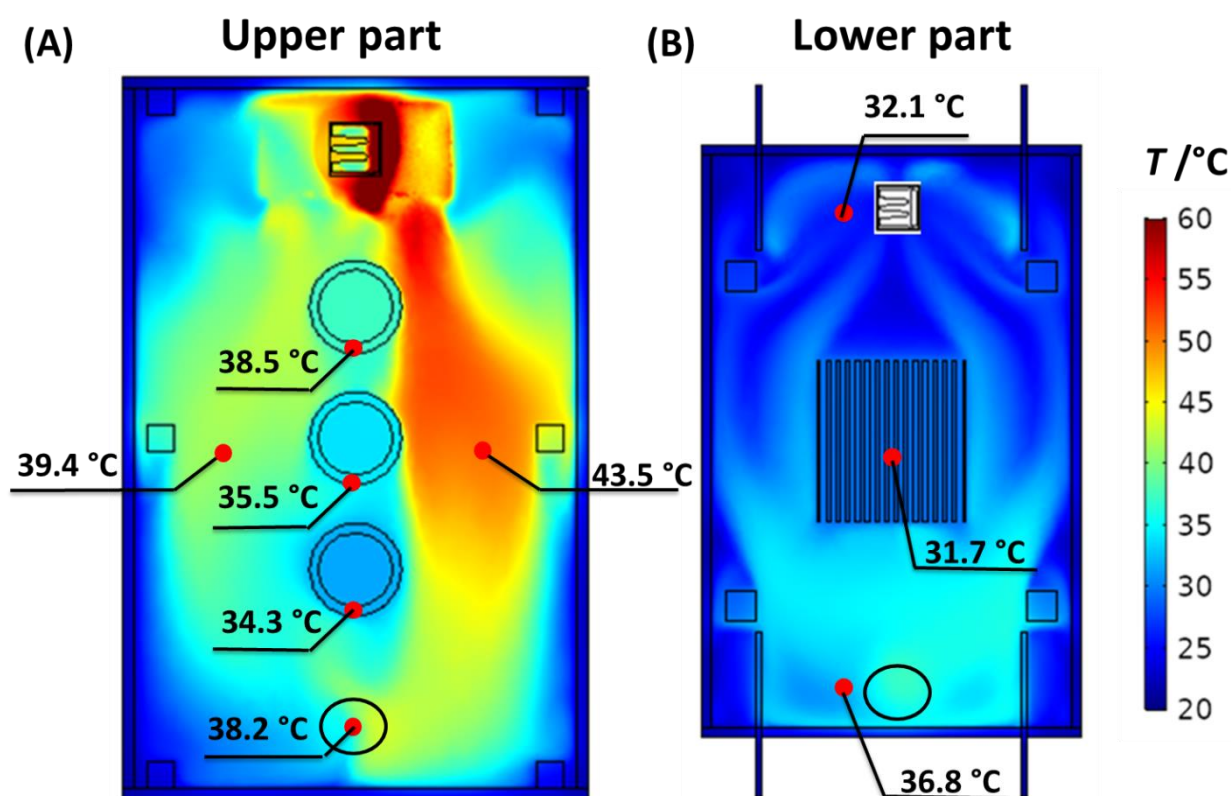
427 9C). The fan heater affects the temperature distribution on the heat sink. Here we can observe a strong
 428 heat accumulation, which consequently influences the temperature on the right side of the heat sink by
 429 convection. Two hotspots on the heat sink can be revealed by the numerical simulation. These
 430 correspond to the position of the two Peltier modules below the heat sink. The temperature distribution
 431 among the channels shown in Fig. 9C is in good agreement with the corresponding numerical data (see
 432 Fig. 7). Additionally, the cooling effect of the auxiliary heat sink becomes visible. As a result, a cold
 433 spot in the right corner of the device is created. The cold air has to be heated up again by the air heater.
 434 In Figure 89D, we compared the numerical solution of the temperature increase measured by the internal
 435 probes with experimental data under laboratory conditions. Numerical simulations showed good
 436 agreement with the experimental data. The setpoint temperature is reached a bit earlier, especially for
 437 the temperature in the inner zone. This can be attributed to better insulation of the numerical model
 438 compared to the real world test system. Additionally, the Peltier modules heat with a constant power in
 439 the numerical model, whereas in the test system the heating power is influenced by the temperature-
 440 dependent Seebeck effect. Further deviations were already discussed and can be mainly attributed to the
 441 poor mesh quality of the air domain.



442

443 **Figure 9:** Surface and volume plots of selected compounds from the complete 3D model obtained by numerical simulations.
 444 **A:** volume plot of the enclosed air volume in the lower part of the channel. **B:** surface plot of a cross-section through the heat
 445 sink. **C:** surface plot of a vertical cross-section through the complete 3D model. **D:** surface plot of a horizontal cross-section
 446 through the upper part.

447 Finally, Fig. 10 compares the numerical results of the steady-state (achieved after 360 min) with the
 448 experimental data from external temperature sensors. The surface plots are combined and mapped to
 449 local temperatures from the external sensors. A qualitative observation shows that numerical results are
 450 in good accordance with experimental data. These results together with the results from Fig. 89
 451 demonstrate the superiority of numerical simulations. On the one hand, using standard laboratory
 452 equipment (*i.e.* mainly temperature sensors) only a few local temperatures can be captured. On the other
 453 hand, numerical simulations provide simultaneously and time-dependent data available at each point
 454 within the considered geometry. Thus, spatial gradients can be visualized.



455
 456 **Figure 10:** Comparison of numerical solutions of the 3D numerical model with experimental data obtained from the IMC test
 457 system under laboratory conditions. **A:** Mapped local temperatures in the upper part of the calorimetric test system. **B:** Mapped
 458 local temperatures in the lower part of the calorimetric test system.

459 Conclusion

460 The design and construction of isothermal microcalorimeters (IMC), whether for special applications or
 461 commercial multipurpose instruments, pose enormous challenges to the developer or manufacturer. Tiny
 462 heat fluxes in the range of a few microwatts or even nanowatts have to be measured. This places the
 463 highest demands on the temperature constancy of an IMC. During the development process of such an
 464 instrument early constructed test systems, prototypes and finally production device are built and tested
 465 under laboratory conditions. From an experimental point of view, only a few parameters such as local
 466 temperatures through e.g. Pt100 sensors, the control behavior of heating or cooling elements and the

467 performance of the heat flow sensors can be recorded. Comprehensive temperature distributions in the
468 entire system or selected components of it, local hotspots and their impact on the performance of the
469 device remain mostly uncovered. However, these are crucial if the overall IMC system is to be
470 optimized.

471 In the present study, we were able to demonstrate that numerical simulations can support experimental
472 data and provide deeper insights into the contribution of single components to the overall performance
473 of the entire system. Based on an IMC test system that is specifically designed for microbiological
474 analysis, we determined in numerical simulations control parameters for a PI controller which regulates
475 the temperature on the heat sink. Further, we investigated the temperature distribution among the
476 channels in the upper part of the 3D model. Here, we simulated the first modifications to investigate
477 their impact on the temperature homogeneity between the channels. Finally, we performed a time-
478 dependent simulation of the complete 3D model to obtain numerical data for the entire system. The
479 advantages of such numerical simulations are:

480 First, the time saved in determining control parameters for the different controller and their interplay.
481 For example, the windup or the influence of individual control variables on the control behavior can be
482 excellently investigated in this way.

483 Second, weak points of a test system can be visualized at an early stage and, depending on the
484 complexity of the 3D model, quantified to a certain extent. In this way, a better understanding of the
485 complex interplay of heat fluxes, temperature distributions and fluid dynamics in the entire IMC system
486 can be achieved.

487 Third, failure to design both specialized and multipurpose IMCs represents not only a considerable delay
488 for the respective research task but also an economic risk. Using simulations, it is conceivable to first
489 design and optimizes an IMC *in silico* and later builds it only if the required performance parameters
490 are predicted.

491 **Acknowledgments**

492 The authors thank the Federal Ministry for Economic Affairs and Energy and the German Federation of
493 Industrial Research Associations for the financial support of this research under the grant number
494 (ZF4315807RH7). We would also like to thank Hartwin Lier (KEK GmbH) for design and construction
495 of the microcalorimetric test system and Bernd Herrmann (UFZ) for the administrative support during
496 the simulations.

497 **Author Contributions**

498 **Christian Fricke:** Conceptualization, Methodology, Investigation, Writing - Original Draft,
499 Visualization, Formal analysis **Sven Richter:** Conceptualization, Software, Resources **Toralf Klee:**
500 Conceptualization, Software, Resources. **Sven Paufler:** Conceptualization, Visualization, Writing -

501 Review & Editing **Hauke Harms**: Supervision, Writing - Review & Editing **Thomas Maskow**:
502 Conceptualization, Supervision, Writing - Review & Editing.
503 All authors reviewed the manuscript and agreed with the content.

504 **Literature**

505

- 506 1. Wadsö, L. Isothermal Microcalorimetry. Current problems and prospects. *Journal of Thermal*
507 *Analysis and Calorimetry* **64**, 75–84 (2001). <https://doi.org/10.1023/A:1011576710913>.
- 508 2. Attree RW, Cushing RL, Ladd JA, Pieroni JJ. Differential Calorimeter of the Tian - Calvet Type.
509 *Review of Scientific Instruments*. **29**, 491-6 (1958). <https://doi.org/10.1063/1.1716233>.
- 510 3. Sarge SM, Höhne G, Hemminger W. *Calorimetry: Fundamentals, Instrumentation and*
511 *Applications*. Wiley-VCH: Weinheim, Germany, 2014.
- 512 4. Calvet E, Prat H. *Recent Progress in Microcalorimetry*. (ed) Skinner HA. Pergamon Press: Oxford.
513 1963.
- 514 5. Wadso I. Design and Testing of a Micro Reaction Calorimeter. *Acta Chemica Scandinavica*. **22**,
515 927-37 (1968). <https://doi.org/10.3891/acta.chem.scand.22-0927>.
- 516 6. Evans WJ, McCourtney EJ, Carney WB. A Microcalorimeter Using Semiconductors as the Sensing
517 Elements. *Instrumentation Science & Technology*. **2**, 249-55 (1969).
518 <http://doi.org/10.1080/10739146908543280>.
- 519 7. Stott JB. An isothermal micro-calorimeter. *Journal of Scientific Instruments*. **33**, 58-63 (1956).
520 <https://doi.org/10.1088/0950-7671/33/2/304>.
- 521 8. Ishikawa Y, Shoda M, Maruyama H. Design and performance of a new microcalorimetric system
522 for aerobic cultivation of microorganisms. *Biotechnology and Bioengineering*. **23**, 2629-40 (1981).
523 <https://doi.org/10.1002/bit.260231118>.
- 524 9. Bauer S, Ploss B. Design and properties of a microcalorimeter. *IEEE Transactions on Electrical*
525 *Insulation*. **27**, 861-6 (1992). <https://doi.org/10.1109/14.155811>.
- 526 10. Moreno-Pirajan JC, Gutierrez LG, Ordonez AG. A batch-type heat conduction microcalorimeter
527 for immersion heat determinations: design, calibration and applications. *Thermochimica Acta*. **290**, 1-
528 12 (1997). [https://doi.org/10.1016/S0040-6031\(96\)03066-3](https://doi.org/10.1016/S0040-6031(96)03066-3).
- 529 11. Wadsö, I., Wadsö, L. A second generation twin double microcalorimeter. *Journal of Thermal*
530 *Analysis and Calorimetry* **49**, 1045–1052 (1997). <https://doi.org/10.1007/BF01996792>
- 531 12. Wadsö I, Hallén D, Jansson M, Suurkuusk J, Wenzler T, Braissant O. A well-plate format
532 isothermal multi-channel microcalorimeter for monitoring the activity of living cells and tissues.
533 *Thermochimica Acta*. **652**, 141-149 (2017). <https://doi.org/10.1016/j.tca.2017.03.010>.
- 534 13. Parrillo DJ, Gorte RJ. Design parameters for the construction and operation of heat-flow
535 calorimeters. *Thermochimica Acta*. **312**, 125-32 (1998). [https://doi.org/10.1016/S0040-6031\(97\)00446-2](https://doi.org/10.1016/S0040-6031(97)00446-2).
- 536

- 537 14. Zhang WS. Construction, calibration and testing of a decimeter-size heat-flow calorimeter.
538 *Thermochimica Acta*. **499**, 128-32 (2010). <https://doi.org/10.1016/j.tca.2009.11.013>.
- 539 15. Chen A-t, Wadsö I. A test and calibration process for microcalorimeters used a thermal power
540 meters. *Journal of Biochemical and Biophysical Methods*. **6**, 297-306 (1982).
541 [https://doi.org/10.1016/0165-022X\(82\)90011-2](https://doi.org/10.1016/0165-022X(82)90011-2).
- 542 16. X. Cui, Y. Li, X. Gao, A new design and evaluation technique of a microcalorimeter, *2012*
543 *Conference on Precision electromagnetic Measurements*, 736-738 (2012).
544 <https://doi.org/10.1109/CPEM.2012.6251140>.
- 545 17. Khaw MK, Mohd-Yasin F, Nguyen NT. Microcalorimeter: Design considerations, materials and
546 examples. *Microelectronic Engineering*. **158**, 107-117 (2016).
547 [doi:https://doi.org/10.1016/j.mee.2016.03.050](https://doi.org/10.1016/j.mee.2016.03.050).
- 548 18. Hansen LD, Russell DJ. Which calorimeter is best? A guide for choosing the best calorimeter for a
549 given task. *Thermochimica Acta*. **450**,71-2 (2006). <https://doi.org/10.1016/j.tca.2006.08.001>.
- 550 19. Suurkuusk, J., Suurkuusk, M. & Vikegard, P. A multichannel microcalorimetric system. *Journal of*
551 *Thermal Analysis and Calorimetry* **131**, 1949–1966 (2018). [https://doi.org/10.1007/s10973-017-6684-](https://doi.org/10.1007/s10973-017-6684-7)
552 [7](https://doi.org/10.1007/s10973-017-6684-7).
- 553 20. Wadso L, Smith AL, Shirazi H, Mulligan SR, Hofelich T. The isothermal heat conduction
554 calorimeter: A versatile instrument for studying processes in physics, chemistry, and biology. *Journal*
555 *of Chemical Education*. **78**, 1080-6 (2001). <https://doi.org/10.1021/ed078p1080>.
- 556 21. Wadso I, Goldberg RN. Standards in isothermal microcalorimetry (IUPAC technical report). *Pure*
557 *and Applied Chemistry*. **73**, 1625-39 (2001). <https://doi.org/10.1351/pac200173101625>.
- 558 22. Giraldo L, Moreno JC. Thermal and Electric Characterization of the Sensor System in the
559 Microcalorimetry of Heat Conduction. *Instrumentation Science & Technology*. **28**, 223-31 (2002).
560 <https://doi.org/10.1081/CI-100100973>.
- 561 23. Rao SS. Chapter 1 - Overview of Finite Element Method. In: Rao SS, editor. *The Finite Element*
562 *Method in Engineering (Fifth Edition)*. Boston: Butterworth-Heinemann; 2011. p. 3-50.
- 563 24. Pepper DW, Heinrich JC. *The finite element method : basic concepts and applications with*
564 *MATLAB, MAPLE, and COMSOL*. 2017.
- 565 25. Vilchiz LE, Pacheco-Vega A, Handy BE. Heat-flow patterns in Tian–Calvet microcalorimeters:
566 Conductive, convective, and radiative transport in gas dosing experiments. *Thermochimica Acta*.
567 **439**,110-8 (2005). <https://doi.org/10.1016/j.tca.2005.09.014>.
- 568 26. Koci V, Madera J, Jerman M, Cerny R. Computational analysis of heat transport and storage
569 processes in large-volume isothermal heat flow calorimeter. *Applied Thermal Engineering*. **121**, 547-
570 53 (2017). <https://doi.org/10.1016/j.applthermaleng.2017.04.118>.
- 571 27. Gonzalez-Duran JEE, Zamora-Antunano MA, Lira-Cortes L, Rodriguez-Resendiz J, Olivares-
572 Ramirez JM, Lozano NEM. Numerical Simulation for the Combustion Chamber of a Reference
573 Calorimeter. *Processes*. **8**, 575 (2020). <https://doi.org/10.3390/pr8050575>.
- 574 28. Oberdorfer P. *How to Save Computational Time with One-Way Coupling Approach*. 2017.
575 Accessed 26.05.2021.

- 576 29. COMSOL Multiphysics®. *CFD Module User's Guide 5.5*.
577 <https://doc.comsol.com/5.5/doc/com.comsol.help.cfd/CFDModuleUsersGuide.pdf>. Accessed
578 26.05.2021.
- 579 30. COMSOL Multiphysics. *The Boussinesq Approximation*. 2015.
580 <https://www.comsol.com/multiphysics/boussinesq-approximation>. Accessed 26.01.2021.